Nanocurved electric-field-induced optimal catalyst loading for carbon dioxide electroreduction

Wenzhao Yu, Huijun Jiang,* and Zhonghuai Hou

Hefei National Research Center for Physical Sciences at the Microscale & Key Laboratory of Precision and Intelligent Chemistry,
University of Science and Technology of China, Hefei, Anhui 230026, China

As a simple way to enhance catalytical performance, it has long been believed that catalyst loading increases the number of sites available for reaction. The overall reaction rate will increase and saturate eventually as catalyst loading increases. Here, we report a counterintuitive optimal catalyst loading for electrocatalytic carbon dioxide reduction (eCO$_2$R) on nanocatalysts. Numerical analysis based on a comprehensive kinetic model reveals that nanocurved electric field (NEF) resulted from the comparable size of nanocatalysts and the electric double layer can essentially affect eCO$_2$R. While NEF induces extra mass transfer raising the overall reaction rate for low catalyst loading, such extra mass transfer is sharply reduced due to the overlap of NEF for high catalyst loading. These findings challenge the conventional physical picture of loading-dependent overall catalytical performance, and provide a new concept for design of nanocatalysis.

I. INTRODUCTION

Carbon dioxide electroreduction (eCO$_2$R) provides an effective way to utilize the growing abundance of renewable electricity from solar, wind, and geothermal energy to transform carbon dioxide into value-added chemicals and fuels [1–7]. To date, great efforts have been made to improve eCO$_2$R by design of the catalyst, the electrode, or electrolyte [8–14]. For example, special catalyst structure of confinement [15–17], intercalation [18,19], alloy [20–22], and core-shell [23,24], and utilization of gas diffusion electrodes [25] and ionic liquids [26,27] were applied. Increasing catalyst loading is a simple method to enhance the overall electrocatalytic performance [28–31]. For instance, Li *et al.* [30] developed a novel MoS$_2$/RGO hybrid material to increase dispersed MoS$_2$, leading to superior electrocatalytic activity. Similarly, Manthiram *et al.* achieved almost 4 times higher reaction rate compared to the copper foil by increasing the copper nanoparticles supported on glassy carbon [31]. It has long been believed that increasing loading of catalysts with fixed dispersion increases the number of sites available for reaction, and thus enhances the overall reaction rate in the intrinsic-activity-controlled region. Further increasing catalyst loading leads the overall reaction into the mass-transfer-controlled region, so that the overall reaction rate saturates eventually at a limited value [32,33]. This conventional picture indicates an important role of mass transfer playing in the overall electrocatalytic performance, and suggests that catalyst loading is the more the better to enhance the overall reaction rate.

Recently, several studies implied that mass transfer may differ from predictions of traditional theories when the catalyst is taken down to nanoscales [34–36]. As the nanocatalyst is of a size comparable to the thickness of electrical double layer, electric field is actually nanocurved near the electrode surface [37–39]. Our previous studies have revealed that the nanocurved electric field (NEF) can lead to an extra mass transfer which further results in nontrivial effects on the overall reaction performance of eCO$_2$R. It has been shown that NEF can enhance electrocatalytic activity of eCO$_2$R by providing extra CO$_2$ on needle-shaped catalysts [40]. NEF can also change the distribution of OH on the electrode surface while keeping pH near the electrode unchanged, indicating a hidden mechanism behind roughness-enhanced high selectivity of carbon monoxide electrocatalytic reduction [41]. It is then very interesting to explore whether NEF is able to change essentially the conventional dependence of electrocatalytic performance on catalyst loading.

In this paper, we address this issue theoretically by a comprehensive kinetic model of eCO$_2$R on nanocatalysts, including adsorption, desorption, diffusion, reduction of CO$_2$, and especially the NEF effect. We find a counterintuitive optimal catalyst loading achieving a maximal overall reaction rate. Detailed analysis shows that NEF near each catalyst in nearly isolated for low catalyst loading. This type of NEF can induce extra mass transfer to enhance the overall reaction rate. For high catalyst loading, such mass transfer is reduced due to the overlap of NEF, and consequently the overall reaction rate decreases. In addition, effects of catalyst loading, catalyst curvature, and randomness of catalyst spatial distribution on eCO$_2$R are also fully explored. It is concluded that catalysts of sharp curvature, moderate loading, and regular spatial arrangement facilitate eCO$_2$R on nanocatalysts.
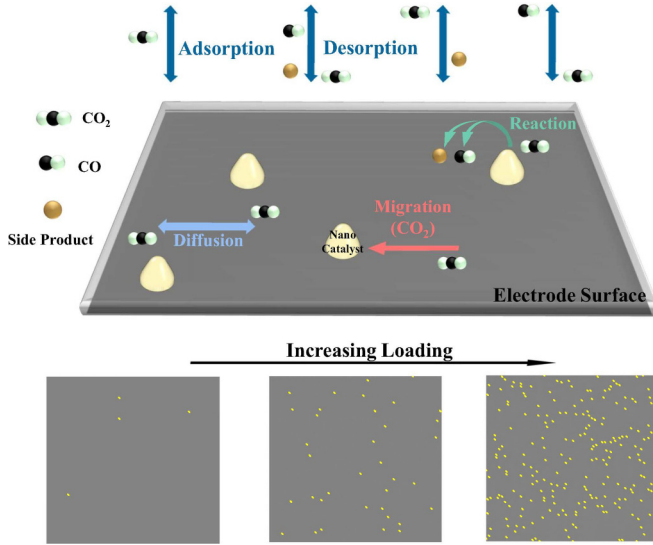
*hjjiang3@ustc.edu.cn

FIG. 1. Illustration of the kinetic model for eCO2R on electrode surface of different catalyst loading. The whole catalytic process includes effective adsorption, desorption, diffusion, reduction of CO_2, and NEF-induced effects. Catalyst loading is changed by varying the number of nanocatalysts (yellow dots in the bottom figure).

II. MODEL AND METHOD

As shown in Fig. 1, we extend our kinetic model of eCO$_2$R on nanocatalysts of different curvature [40–42] to explore eCO$_2$R on an electrode of different catalyst loading. Key stages of the whole catalytic process are considered, including effective adsorption, desorption, diffusion, reduction of CO_2, and especially the NEF effect. The reaction-diffusion equations governing the evolution of surface concentrations are as follows:

$$\frac{\partial \theta_{\mathbf{r}}^{co_2}}{\partial t} = k_{ad}^{co_2}\left(1 - \theta_{\mathbf{r}}^{co_2}\right) - k_d^{co_2}\theta_{\mathbf{r}}^{co_2} + D^{co_2}\nabla^2\theta_{\mathbf{r}}^{co_2}$$
$$+ \frac{D^{co_2}}{k_B T}\nabla \cdot \left[\theta_{\mathbf{r}}^{co_2}\left(1 - \theta_{\mathbf{r}}^{co_2}\right)\nabla\left(\partial_{\theta^{co_2}}\sum_{i=1}^{n_c}V_{\mathbf{r}}^{i,co_2}\right)\right]$$
$$- k_{\eta=0}^{co}\exp(\lambda^{co}\eta^{co})\theta_{\mathbf{r}}^{co_2} - k_{\eta=0}^{sp}\exp(\lambda^{sp}\eta^{sp})\theta_{\mathbf{r}}^{co_2}, \quad (1)$$

$$\frac{\partial \theta_{\mathbf{r}}^{co}}{\partial t} = k_{\eta=0}^{co}\exp(\lambda^{co}\eta^{co})\theta_{\mathbf{r}}^{co_2} - k_d^{co}\theta_{\mathbf{r}}^{co} + D^{co}\nabla^2\theta_{\mathbf{r}}^{co}, \quad (2)$$

$$\frac{\partial \theta_{\mathbf{r}}^{sp}}{\partial t} = k_{\eta=0}^{sp}\exp(\lambda^{sp}\eta^{sp})\theta_{\mathbf{r}}^{co_2} - k_d^{sp}\theta_{\mathbf{r}}^{sp} + D^{sp}\nabla^2\theta_{\mathbf{r}}^{sp}. \quad (3)$$

In the above equations, quantities with superscript CO$_2$, CO, or sp indicate corresponding ones for CO$_2$, CO, or possible side product. k_B is the Boltzmann constant, T is the temperature, $\theta_{\mathbf{r}}$ is the surface concentration of each chemical species at location $\mathbf{r}$, and n_c is the total number of nanocatalysts.

The first (second) term in the right side of Eq. (1) describes the adsorption (desorption) of CO$_2$ where k_{ad} (k_d) is the adsorption (desorption) rate constant. The third and fourth terms describe mass transfer on the electrode surface consisting of normal diffusion with diffusion constant D and the mass transfer induced by NEF [40]. A Gaussian-type effective interaction potential $V_{\mathbf{r}}^{i,co_2} = -\alpha\theta_{\mathbf{r}}^{co_2}U_{\text{tip},i}\exp(-|\mathbf{r} - \mathbf{r}_{\text{tip},i}|^2/r_0^2)$

TABLE I. Kinetic parameters for the simulation of eCO2R on surface of different catalyst loading.

Parameter	$k_{ad}^{co_2}$	$k_d^{co_2}$	k_d^{co}	k_d^{sp}	N	α	r_0
Value	0.1	9.9	10.0	10.0	120	1.0	5.0
Parameter	$k_{\eta=0}^{co}$	$k_{\eta=0}^{sp}$	D^{co}	D^{sp}	λ^{co}	λ^{sp}	
Value	100.0	5.0	1.0	1.0	1.5	0.75	

is applied to approximate the effective interaction between the NEF of the ith catalyst and CO$_2$ locating at $\mathbf{r}$ (with the help of K$^+$)[40], where α is the interaction strength, r_0 is the characteristic length of the potential, $r_{\text{tip},i}$ is the location of the catalyst, and $U_{\text{tip},i}$ is the intensity of NEF depending on the ith catalyst's curvature radius $R_{\text{tip},i}$. The relationship between $U_{\text{tip},i}$ and $R_{\text{tip},i}$ is $U_{\text{tip},i}(R_{\text{tip},i}) = (u_0/u_p)(R_{\text{tip},i}/R_p)^{-0.7}$ [40], where u_0 is the applied electrode potential, u_p and R_p are electrode potential (-0.35 V versus RHE) and curvature radius of the spherical catalyst in Liu's experiments [43]. Then, u_0 keeps the same as u_p, at which H$_2$ evolution reaction exhibited very low current density, and the size of nanocatalysts varies above quantum size regime to avoid the significance of quantum size effects. Additionally, two reactions converting CO$_2$ to the main product CO or side product are included. The fifth and sixth terms describe the reaction rates based on the Butler-Volmer equation [44], where $k_{\eta=0}^{co}(k_{\eta=0}^{sp})$, $\lambda^{co}(\lambda^{sp})$, and $\eta^{co}(\eta^{sp})$ are the rate constant at equilibrium potential, the apparent barrier-reducing coefficient, and the overpotential for the main (side) reaction, respectively. Considering the side reaction always happens along with the main reaction, the side reaction is considered to happen within an area of radius $r_s = 4r_0$ around the catalyst by taking the area for main reaction as one grid [40]. Similarly, the first, second, and third terms on the right side of Eq. (2) and Eq. (3) are the reaction, desorption, and normal diffusion, respectively. Detailed discussion about the model can be found in the Appendix.

In simulations, Eqs. (1)–(3) are discretized on a lattice of $N \times N$ grids with grid length L and periodic boundary conditions. Kinetic parameters are listed in Table I according to Ref. [40], where $k_B T$, L, and D^{co_2} are chosen as basic units for parameter dimensionless. In each simulation, n_c nanocatalysts of the same curvature are regularly arranged on the electrode surface. Catalyst loading n measured by $n = n_c/(N*N)$ can be strictly correlated with the available number of active sites for reaction as the size of each dispersed nanocatalyst keeps the same. The effect of catalyst distribution is further explored at the end of the result part. The overall producing rate of CO is measured by $v = \sum_i \sum_j v_{ij}$, where v_{ij} represents the main reaction rate on the (i, j) grid.

III. RESULTS

Time series of the overall producing rate v for the main product on catalysts of two typical curvature radii $R_{\text{tip}}/R_p = 0.9$ and 0.3 and three different catalyst loading $n = 0.00694$, 0.01, and 0.01563 are plotted in Figs. 2(a) and 2(b), respectively. It can be found that v eventually reaches a steady state after a short transient state, thus all of the following results are obtained in the steady state. In Fig. 2(a), v is
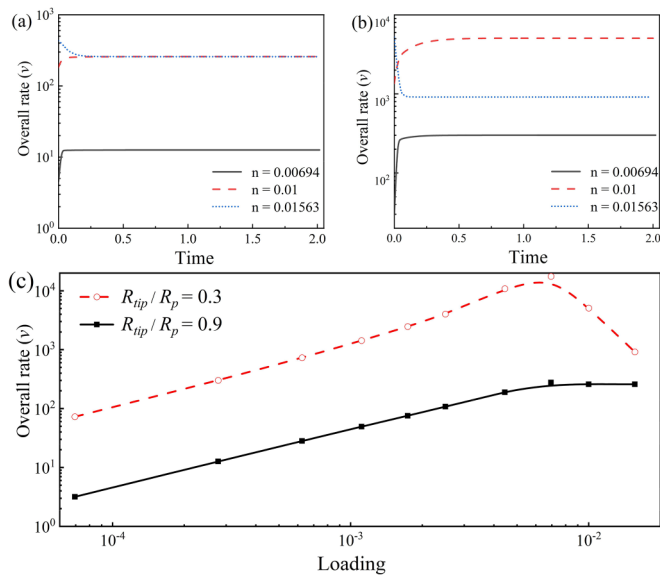
FIG. 2. Time series of the overall rate of the main reaction v on two typical catalysts of curvature radius $R_{tip}/R_p =$ (a) 0.9 and (b) 0.3, respectively, where catalyst loading is $n = 0.00694$, 0.01, and 0.01563. (c) Dependence of v on the catalyst loading n on catalysts of curvature radius $R_{tip}/R_p = 0.9$ and 0.3.

smaller for $n = 0.00694$ than that for $n = 0.01$ and 0.01563, and is almost the same for $n = 0.01$ and 0.01563, indicating that the overall reaction rate increases and saturates as catalyst loading increases. However, v is obviously smaller for $n = 0.01563$ than that for $n = 0.01$ when catalysts are of a sharp curvature $R_{tip}/R_p = 0.3$ as shown in Fig. 2(b).

To show this quantitatively, dependence of the overall producing rate v on the catalyst loading n for $R_{tip}/R_p = 0.9$ and 0.3 are plotted in Fig. 2(c). Three observations can be concluded. Firstly, dependence of v on n on catalysts of $R_{tip}/R_p = 0.9$ is similar to the conventional one mentioned in the introduction section. That is, v first increases and then saturates eventually at a limited value as n increases. Secondly, v is always larger on catalysts of $R_{tip}/R_p = 0.3$ than on those of $R_{tip}/R_p = 0.9$ when n is the same, meaning that catalysts of sharper curvature can enhance the reaction. This observation is consistent with previous findings in literature [40]. Lastly and interestingly, v of $R_{tip}/R_p = 0.3$ increases for small ns, but turns to decrease when n is larger than an optimal value n_0. Such an optimal catalyst loading for eCO$_2$R is quite different from the conventional understanding of loading-dependent catalytical performance. We notice that similar phenomena were also reported in recent experiments [45,46], implying that there can be new physics for loading-dependent catalysis at nanoscales.

In order to reveal the mechanism underlying optimal catalyst loading for eCO$_2$R on nanocatalysts, averaged CO$_2$ concentration $\bar{\theta}^{co_2}$ on the electrode surface is plotted in Fig. 3(a). It can be seen that $\bar{\theta}^{co_2}$ of $R_{tip}/R_p = 0.3$ is always higher than that of $R_{tip}/R_p = 0.9$, which is inconsistent with previous reported enhancement of eCO$_2$R by NEF-induced extra mass transfer [40]. Besides, a clearcut drop for $R_{tip}/R_p = 0.3$ is observed when catalyst loading is larger than n_0.
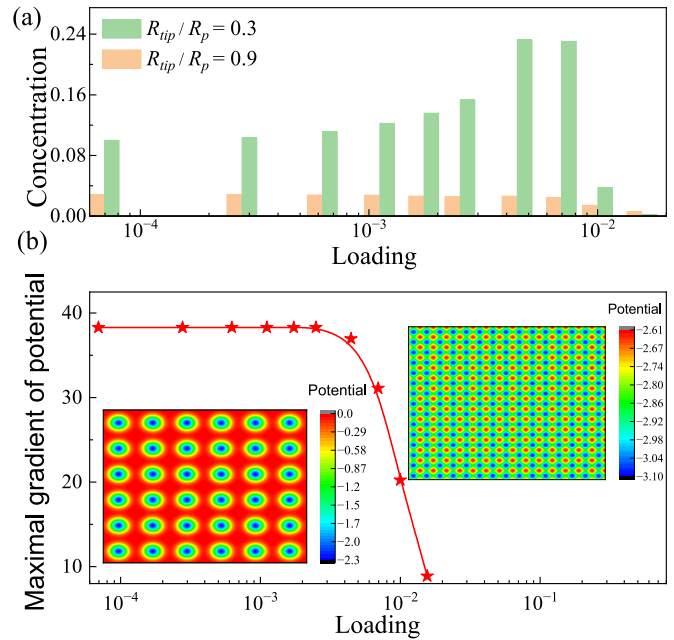

FIG. 3. Mechanism of NEF-induced optimal catalyst loading for eCO$_2$R performance. (a) Dependence of the mean surface concentration of CO$_2$ on catalyst loading for catalyst of sharp and smooth curvatures. (b) The absolute value of the maximum gradient of the effective potential as a function of catalyst loading. The left and right inset are the potential distribution with low ($n = 0.0025$) and high catalyst loading ($n = 0.01563$), respectively.

Then, the key point turns to understanding why increasing catalyst loading leads to low CO$_2$ concentration on the surface when n is large enough. Spatial distributions of interaction potential between NEF and CO$_2$ with low ($n = 0.0025$) and high catalyst loading ($n = 0.01563$) are shown in the left and right insets in Fig. 3(b), respectively. Potential wells of low catalyst loading are separated clearly with each other, while ones of high catalyst loading are overlapped obviously. As described in Eq. (1), NEF-induced mass transfer is always along the reverse direction of the gradient of the interaction potential. Overlap of potential wells may reduce the intensity of potential gradient, which further decreases NEF-induced mass transfer. Dependence of the maximum absolute value of the potential gradient g on catalyst loading n is plotted in Fig. 3(b). It is observed that g remains unchanged when n is small, indicating the increase of overall reaction rate is solely a result of increasing the number of sites available for eCO$_2$R. When n is large, g declines sharply due to highly overlapped potential, which then reduces the NEF-induced mass transfer. In short, the competition between increasing number of reaction sites and decreasing NEF-induced mass transfer results in the counterintuitive optimal catalyst loading for eCO$_2$R performance.

To fully explore how the NEF-induced mass transfer affects eCO$_2$R performance, intensive simulations are performed to obtain the overall reaction rate on the n-R_{tip} plane. As shown in Fig. 4(a), NEF-induced optimal catalyst loading for eCO$_2$R performance appears on catalysts of high curvatures (small curvature radius). However, v may decrease again if the curvature radius of catalysts is too small. High eCO$_2$R
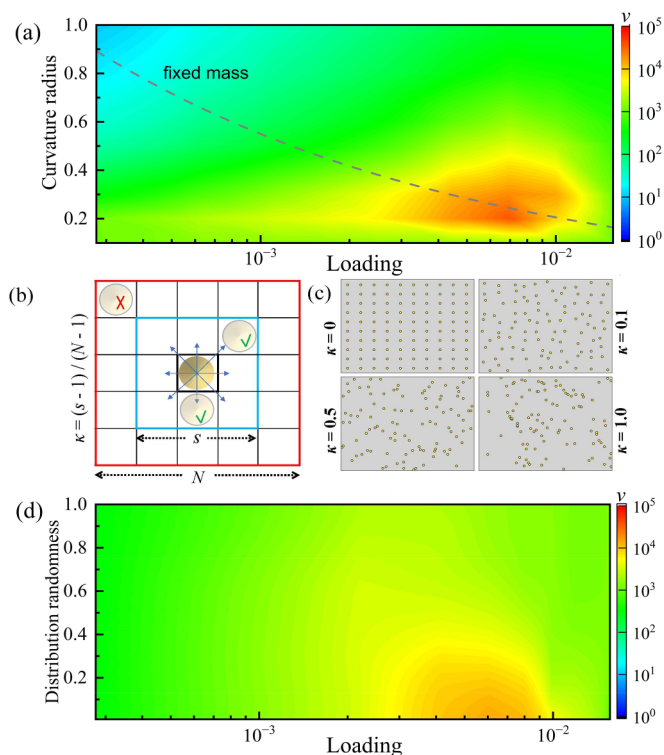
FIG. 4. (a) The overall reaction rate on the loading-curvature plane with regularly assigned catalysts. The dot line indicates nanocatalysts of different curvature when the total catalyst mass keeps constant. (b) The schematic for generating a random catalyst distribution according to a randomness κ. (c) Typical configuration for $\kappa = 0$ (upleft), 0.1 (upright), 0.5 (downleft), and 1.0 (downright) in $n = 0.00694$. (d) The overall reaction rate on the loading-randomness plane with fixed $R_{tip}/R_p = 0.3$. Color bars indicate the value of the overall rate.

performance can be achieved in a parameter region of not too high catalyst loading and not too small curvature radius. It is well known that dispersion is also critical to the overall reaction rate by increasing the number of reaction sites, which implies that the radius of nanocatalysts should always be as small as possible to maximize the overall reaction rate. For a given mass of catalysts, the size of nanocatalysts is inversely proportional to the cubic root of the number of nanocatalysts $R_{tip} \propto n_c^{-1/3}$ as dispersion changes. To show that the NEF-induced optimal loading is not simply an effect of changing catalyst dispersion, dependence of the overall reaction rate on the curvature radius of nanocatalysts when the total catalyst mass keeps constant is indicated by the dotted line (taking the proportionality coefficient as 1 for example) in Fig. 4(a). Clearly, the overall rate also shows a maximal value as dispersion changes, demonstrating again that the NEF-induced enhancement does present new physics about nanoelectrocatalysis.

In Fig. 4(d), effect of catalyst spatial distribution on the overall reaction rate of eCO$_2$R is presented on the n-κ plane with fixed $R_{tip}/R_p = 0.3$. Here, $\kappa = (s-1)/(N-1)$ measures the randomness of catalyst distribution with s a number varying in the range $[1, N]$. As shown in Fig. 4(b), catalyst distribution for a given κ is generated as follows.

Firstly, catalysts are arranged regularly on the electrode surface. Then, each catalyst is moved to a random position in the square of size s centered on its original position in the regular arrangement. Typical configuration for for $\kappa = 0$ (upleft), 0.1 (upright), 0.5 (downleft), and 1.0 (downright) when $n = 0.00694$ are presented in Fig. 4(c). The spatial distribution is regular for $\kappa = 0$, and completely random for $\kappa = 1$. Here, the overall rate of the main reaction v is further averaged over an ensemble of 10 samples for $\kappa > 0$. It can be seen that v decreases gradually as the catalyst distribution becomes more random, which agrees with the observation reported previously that regular distribution can enhance electrocatalysis by NEF-induced extra mass transfer [42]. It can be concluded from the phase diagrams in Figs. 4(a) and 4(b) that, in catalysts of sharp curvature (but not too sharp), moderate loading and regular spatial arrangement facilitate eCO$_2$R at nanoscales.

In summary, effects of catalyst loading on electrocatalytical carbon dioxide reduction (eCO$_2$R) at nanoscales have been investigated numerically by a comprehensive kinetic model. It was found that nanocurved electric field (NEF) near each catalyst is nearly isolated for low catalyst loading, which induces extra mass transfer raising the overall reaction rate. For high catalyst loading, however, the extra mass transfer decreases sharply due to the overlap of NEF, leading to a decline of the overall rate. Competition between these two effects thus results in a counterintuitive optimal catalyst loading for eCO$_2$R on nanocatalysts. We believe that the findings challenge the conventional physical picture of loading-dependent overall catalytical performance and provide a new concept for design of nanocatalysis.

APPENDIX A: DETAIL OF THE REACTION-DIFFUSION EQUATIONS FOR THE KINETIC MODEL

The first term in the right side of Eq. (1) describes the effective adsorption of CO$_2$ with a rate constant $k_{ad}^{co_2}$ from the solution bulk to the surface, which compacts CO$_2$ diffusion across the solution bulk to the neighborhood of the electrode and adsorption of the nearby CO$_2$ to the electrode surface. The adsorbed CO2 can also desorb from the surface back into the solution with a rate constant $k_d^{co_2}$ [the second term in the right side of Eq. (1)]. Such a pair of reversible processes determines the equilibrium surface concentration of CO$_2$ as $\theta_{eq} = \frac{k_{ad}}{k_{ad}+k_d}$ for a bare surface without any follow-up reactions. It is known that CO$_2$ is hard to adhere on the electrode surfaces even though alkali metal cations are added, thus, θ_{eq} should be very small as well as $k_{ad}^{co_2}$.

Differing from a conventional reaction-diffusion system, the high-curvature-catalyst-enhanced local electric field can even lead to extra mass transfer of CO$_2$ with the help of K$^+$, [43] which may be from the solution bulk to the elec-

trode or from other parts of the electrode surface towards the high-curvature catalysts. Since the former is usually very limited [47], we mainly consider the latter in the kinetic model as the fourth term in the right side of Eq. (1) with V an effective potential due to the interaction between CO_2 and the electric field. Although the exact form of the potential is still unknown, we choose, to the first order of approximation, a Gaussian interaction potential as $V_{\mathbf{r}}^{i,co_2} = -\alpha\theta_{\mathbf{r}}^{co_2}U_{\text{tip},i}\exp(-|\mathbf{r}-\mathbf{r}_{\text{tip},i}|^2/r_0^2)$, where α is the interaction strength, r_0 measures the characteristic length of the potential, $\mathbf{r}_{\text{tip},i}$ means the location of the nanocatalysts, and $U_{\text{tip},i}$ is the intensity of the local nanocurved electric field (NEF) depending on the ith relative catalyst's curvature radius $R_{\text{tip},i}/R_p$. This approximation is quite reasonable due to the following two basic facts: Firstly, for a fixed K^+ concentration, the charge of CO_2 at location $\mathbf{r}$ is proportional to the corresponding CO_2 concentration, thus resulting in a potential proportional to θ_{CO_2}; Secondly, the potential should be of its extremum at the catalyst and vanish away from the catalyst. The electrostatic field intensity $U_{\text{tip},i}$ at the catalyst as a function of the relative catalyst's curvature radius $R_{\text{tip},i}/R_p$ can be fitted by using the data given in Ref. [43], which is $U_{\text{tip},i}(R_{\text{tip},i}) = (u_0/u_p)(R_{\text{tip},i}/R_p)^{-0.7}$, where u_0 is the applied electrode potential, u_p and R_p are the electrode potential and the size of the catalyst's curvature radius in the system with spherical particles on Au electrode surface as that in Ref. [43]. For example, u_p is the applied electrode potential in the experiment of sharp-tip enhanced eCO_2R (about -0.35 V versus RHE), and R_p is the corresponding curvature radius of the Au spherical particles. The size of nanocatalysts varies above quantum size regime to avoid the significance of quantum size effects. Here and in other parts of the paper, u_0 keeps the same as u_p, at which H_2 evolution reaction exhibited very low current density and quantities with subscript "p" denote the corresponding quantities in the same reference system.

The normal diffusion of the adsorption CO_2 on the electrode surface can be described by the Fick's law with a diffusion coefficient [the third term in the right side of Eq. (1)]. The electrocatalytic reduction reaction of CO_2 to the main product CO, $CO_2 \rightarrow CO$, is described by the fifth term in the right side of Eq. (1), where $k_{\eta=0}^{co}$ is the reaction rate constant at equilibrium potential. Along with the main reaction, there are also other side reactions leading to the leakage of adsorbed CO_2. In this model, these reactions are compacted into an effective reaction as $CO_2 \rightarrow SP$ with a rate constant $k_{\eta=0}^{sp}$ [the sixth term in the right side of Eq.(1)], where SP stands for the side product. It is noted that the catalysts of high curvature on the electrode surface can induce a locally enhanced electric field U. Both of the main and the side reactions can be accelerated by the electronic field as $k_{\eta=0}^{CO(sp)}\exp(\lambda^{CO(sp)}\eta^{CO(sp)}(U))\theta_{\mathbf{r}}^{CO_2}$, where $\lambda^{CO(sp)}$ and $\eta^{CO(sp)}(U)$ are the apparent barrier-reducing coefficient and the overpotential of the main (side) reaction, respectively. Since eCO_2R suffers from slow kinetics, the main reaction should be quicker relative to other kinetic processes such as adsorption or diffusion of CO_2 on the electrode surface.

As described in Eqs. (2) and (3), the main product CO and side product SP can be generated by the reactions $CO_2 \rightarrow$

TABLE II. The detailed kinetic processes of the model. Here, (s) stands for the species in near surface.

Adsorption	$CO_2 \xrightarrow{k_{ad}^{CO_2}} CO_2$
Desorption	$CO_2 \xrightarrow{k_d^{CO_2}} CO(s)$
	$CO \xrightarrow{k_d^{CO}} CO(s)$
	$SP \xrightarrow{k_d^{SP}} SP(s)$
Diffusion	$CO_2 \xrightarrow{D_{CO_2}} CO_2$
	$CO \xrightarrow{D_{Co}} CO$
	$SP \xrightarrow{D_{SP}} SP$
Reaction	$CO_2 \xrightarrow{k_{CO}} CO$
	$CO_2 \xrightarrow{k_{SP}} SP$
Migration (LMT)	$CO_2 \xrightarrow{V_{CO_2}} CO_2$

CO and $CO_2 \rightarrow SP$ (the first terms in the right sides), and further detached from the electrode surface with rate constants k_d^{CO} and k_d^{sp} (the second terms in the right sides), respectively. The third terms describe normal diffusion of CO and SP with diffusion constants D_{CO} and D_{sp}. Due to the experimental fact that there is no observation of field-induced concentration of CO or other products on the catalysts, the interaction between these products and the electric field is thus neglected. All of the processes can be concluded as expressions in Table II as follows.

APPENDIX B: SIMULATION DETAILS

In simulations, the $L \times L$ electrode surface is discretized to be a rectangle $N \times N$ lattice, and the kinetic equations Eqs. (1)–(3) are solved numerically with periodic boundary conditions. The same reference system with subscript "p" was used for our further simulations.

The dependence of the electrostatic field intensity at the nanocatalysts U_{tip} on the relative catalyst's curvature radius R_{tip}/R_p can be fitted as $U_{\text{tip},i}(R_{\text{tip},i}) = (u_0/u_p)(R_{\text{tip},i}/R_p)^{-0.7}$ by using data in Ref. [43]. Based on the same reference system, u_0/u_p was considered as 1.0 for a same applied electrode potential. Thus, U_{tip} was obtained by the fitting function with a given R_{tip}/R_p. Then, this electrostatic field induced an effective attraction potential for CO_2 towards the catalysts. Since the exact spatial distribution of $V(\mathbf{r})$ is not known, here we choose a Gaussian interaction potential to the first order of approximation as

$$V_{\mathbf{r}}^{i,co_2} = -\alpha\theta_{\mathbf{r}}^{co_2}U_{\text{tip},i}\exp\left(-|\mathbf{r}-\mathbf{r}_{\text{tip},i}|^2/r_0^2\right),$$

where α is the interaction strength and r_0 measures the characteristic length of the potential. Since CO_2 can be attracted to the ith catalyst with the help of K^+, we take $V_{\mathbf{r}}^{i,co_2} > 0$, namely, the $\alpha < 0$ in our simulations.

Furthermore, the electrode potential' effect on reaction rates was considered based on the Butler-Volmer equation. Generally, electrocatalytic reduction reactions are pairs of reversible ones as

$$O \underset{k_b}{\overset{k_f}{\rightleftharpoons}} R$$

and there is a threshold u_e, which the electrode potential needs to be smaller than, to start the electrocatalytic reduction reaction where u_e is also called the equilibrium potential. The net reaction rate is

$$v^{\text{net}} = k_{\eta=0}^f \exp(-\lambda^f \eta)\theta^O - k_{\eta=0}^b \exp(-\lambda^b \eta)\theta^R,$$

where $\eta = u - u_e$ is the overpotential and $\sum_i U_{\text{tip},i} \exp(-|\mathbf{r} - \mathbf{r}_{\text{tip},i}|^2/r_0^2)$ is the electric potential. $k_{\eta=0}^f(k_{\eta=0}^b)$, $\lambda^f(\lambda^b)$, $\theta^O(\theta^R)$ are the rate constant at the equilibrium potential, namely the $\eta = 0$, the apparent barrier-reducing coefficient, and the reagent concentration of the forward (backward) reaction. For a reduction potential $\eta_i < 0$, v_i^{net} is dominated by the forward reaction, and will be zero for $\eta_i \geqslant 0$.

Based on discussion above, in our manuscript, we considered eCO_2R as two reactions happening on the Au electrode—the main reaction to CO and side reaction to possible side products (SP). The main reaction is

$$CO_2 \rightarrow CO.$$
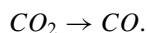
The reaction rate with local potential u based on the Butler-Volmer equation can be written as

$$v = k_{\eta=0}^{CO} \exp(-\lambda^{CO} \eta^{CO})\theta_{\mathbf{r}}^{CO_2}.$$

Similar to the main reaction, the general side reaction to SP is

$$CO_2 \rightarrow SP,$$
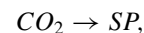
and the side reaction rate can also be written as

$$v_{SP} = k_{\eta=0}^{SP} \exp(-\lambda^{SP} \eta^{SP})\theta_{\mathbf{r}}^{CO_2}.$$

In this way, the overpotential η, shown in equation of two reaction rate above, is $u_{\mathbf{r}} - u_e$ where $u_e = 1.0$ for the main and side reaction and $u_{\mathbf{r}}$ is the local electric potential at the location $\mathbf{r}$, $u_{\mathbf{r}} = U_{\text{tip},i} \exp(-\frac{|\mathbf{r}-\mathbf{r}_{\text{tip},i}|^2}{r_0^2})$. Furthermore, considering the overlap of the local nanocurved electric field with increasing catalyst loading, the absolute intensity of electric potential was enhanced which calculated by linear summation. According to the previous reports, catalysts with high curvature will induce high local electric field and further affect the intrinsic reactivity. Thus, the range of grids on which the reduction reaction can happen is truncated around the catalysts. Notice that the side reaction always happens along with the main reaction; it is reasonable to assume that the range of grid around the catalysts for the side reaction should be larger than that for the main reaction. By taking the area for the main reaction as one grid, i.e., the grid where the catalysts are located, the side reaction can then happen within an area around the catalysts with a size r_s, set as $4r_0$ in our simulation. Moreover, since the exact spatial distribution of the electrode potential is unknown, reaction rate of each grid on which the reaction can happen is considered to be uniform.

[1] M. E. Zick, S. M. Pugh, J.-H. Lee, A. C. Forse, and P. J. Milner, Carbon dioxide capture at nucleophilic hydroxide sites in oxidation-resistant cyclodextrin-based metal–organic frameworks, Angew. Chem., Int. Ed. **61**, e202206718 (2022).

[2] A. R. Woldu, Z. Huang, P. Zhao, L. Hu, and D. Astruc, Electrochemical CO_2 reduction (CO_2RR) to multi-carbon products over copper-based catalysts, Coord. Chem. Rev. **454**, 214340 (2022).

[3] G. Wang, J. Chen, Y. Ding, P. Cai, L. Yi, Y. Li, C. Tu, Y. Hou, Z. Wen, and L. Dai, Electrocatalysis for CO_2 conversion: From fundamentals to value-added products, Chem. Soc. Rev. **50**, 4993 (2021).

[4] W. Ma, X. He, W. Wang, S. Xie, Q. Zhang, and Y. Wang, Electrocatalytic reduction of CO_2 and CO to multi-carbon compounds over Cu-based catalysts, Chem. Soc. Rev. **50**, 12897 (2021).

[5] S. Jin, Z. Hao, K. Zhang, Z. Yan, and J. Chen, Advances and challenges for the electrochemical reduction of CO_2 to CO: From fundamentals to industrialization, Angew. Chem., Int. Ed. **133**, 20795 (2021).

[6] T. Kim and G. T. R. Palmore, A Scalable method for preparing Cu electrocatalysts that convert CO_2 into C_{2+} products, Nat. Commun. **11**, 3622 (2020).

[7] S. Liu, H. Tao, L. Zeng, Q. Liu, Z. Xu, Q. Liu, and J.-L. Luo, Shape-dependent electrocatalytic reduction of CO_2 to CO on triangular silver nanoplates, J. Am. Chem. Soc. **139**, 2160 (2017).

[8] H. Rabiee, L. Ge, X. Zhang, S. Hu, M. Li, and Z. Yuan, Gas diffusion electrodes (GDEs) for electrochemical reduction of carbon dioxide, carbon monoxide, and dinitrogen to value-added products: A review, Energy Environ. Sci. **14**, 1959 (2021).

[9] D. Gao, R. M. Arán-Ais, H. S. Jeon, and B. Roldan Cuenya, Rational catalyst and electrolyte design for CO_2 electroreduction towards multicarbon products, Nat. Catal. **2**, 198 (2019).

[10] E. W. Lees, B. A. Mowbray, F. G. Parlane, and C. P. Berlinguette, Gas diffusion electrodes and membranes for CO_2 reduction electrolysers, Nat. Rev. Mater. **7**, 55 (2022).

[11] L. Fan, C. Xia, F. Yang, J. Wang, H. Wang, and Y. Lu, Strategies in catalysts and electrolyzer design for electrochemical CO_2 reduction toward C_{2+} products, Sci. Adv. **6**, eaay3111 (2020).

[12] R. M. Arán-Ais, D. Gao, and B. Roldan Cuenya, Structure- and electrolyte-sensitivity in CO_2 electroreduction, Acc. Chem. Res. **51**, 2906 (2018).

[13] E. V. Kondratenko, G. Mul, J. Baltrusaitis, G. O. Larrazábal, and J. Pérez-Ramírez, Status and perspectives of CO_2 conversion into fuels and chemicals by catalytic, photocatalytic and electrocatalytic processes, Energy Environ. Sci. **6**, 3112 (2013).

[14] J. H. Montoya, L. C. Seitz, P. Chakthranont, A. Vojvodic, T. F. Jaramillo, and J. K. Nørskov, Materials for solar fuels and chemicals, Nat. Mater. **16**, 70 (2017).

[15] F. Pan, W. Deng, C. Justiniano, and Y. Li, Identification of champion transition metals centers in metal and

nitrogen-codoped carbon catalysts for CO_2 reduction, Appl. Catal., B **226**, 463 (2018).

[16] Q. Hu, Z. Han, X. Wang, G. Li, Z. Wang, X. Huang, H. Yang, X. Ren, Q. Zhang, J. Liu *et al.*, Facile synthesis of sub-nanometric copper clusters by double confinement enables selective reduction of carbon dioxide to methane, Angew. Chem., Int. Ed. **59**, 19054 (2020).

[17] X. Wang, Z. Wang, F. P. García de Arquer, C.-T. Dinh, A. Ozden, Y. C. Li, D.-H. Nam, J. Li, Y.-S. Liu, J. Wicks *et al.*, Efficient electrically powered CO_2-to-ethanol via suppression of deoxygenation, Nat. Energy **5**, 478 (2020).

[18] Q. Zhang, A. He, Y. Yang, J. Du, Z. Liu, and C. Tao, Plasma-activated coox nanoclusters supported on graphite intercalation compounds for improved CO_2 electroreduction to formate, J. Mater. Chem. A **7**, 24337 (2019).

[19] L. Zou, R. Li, Z. Wang, F. Yu, B. Chi, and J. Pu, Synergistic effect of Cu-$La_{0.96}Sr_{0.04}Cu_{0.3}Mn_{0.7}O_{3-\delta}$ heterostructure and oxygen vacancy engineering for high-performance Li-CO_2 batteries, Electrochim. Acta **395**, 139209 (2021).

[20] H. S. Jeon, J. Timoshenko, F. Scholten, I. Sinev, A. Herzog, F. T. Haase, and B. Roldan Cuenya, Operando insight into the correlation between the structure and composition of CuZn nanoparticles and their selectivity for the electrochemical CO_2 reduction, J. Am. Chem. Soc. **141**, 19879 (2019).

[21] Y. Mun, S. Lee, A. Cho, S. Kim, J. W. Han, and J. Lee, Cu-Pd alloy nanoparticles as highly selective catalysts for efficient electrochemical reduction of CO_2 to CO, Appl. Catal., B **246**, 82 (2019).

[22] J. Hao, Z. Zhuang, J. Hao, K. Cao, Y. Hu, W. Wu, S. Lu, C. Wang, N. Zhang, D. Wang *et al.*, Strain relaxation in metal alloy catalysts steers the product selectivity of electrocatalytic CO_2 reduction, ACS Nano **16**, 3251 (2022).

[23] K. Ye, Z. Zhou, J. Shao, L. Lin, D. Gao, N. Ta, R. Si, G. Wang, and X. Bao, In Situ reconstruction of a hierarchical Sn-Cu/SnOx Core/Shell catalyst for high-performance CO_2 electroreduction, Angew. Chem., Int. Ed. **59**, 4814 (2020).

[24] Y. Zhu, X. Cui, H. Liu, Z. Guo, Y. Dang, Z. Fan, Z. Zhang, and W. Hu, Tandem catalysis in electrochemical CO_2 reduction reaction, Nano Res. **14**, 4471 (2021).

[25] J.-B. Vennekoetter, R. Sengpiel, and M. Wessling, Beyond the catalyst: How electrode and reactor design determine the product spectrum during electrochemical CO_2 reduction, Chem. Eng. J. **364**, 89 (2019).

[26] B. A. Rosen and I. Hod, Tunable molecular-scale materials for catalyzing the low-overpotential electrochemical conversion of CO_2, Adv. Mater. **30**, 1706238 (2018).

[27] B. Gu, H. Su, X. Chu, Q. Wang, H. Huang, J. He, T. Wu, W. Deng, H. Zhang, and W. Yang, Rationally assembled porous carbon superstructures for advanced supercapacitors, Chem. Eng. J. **361**, 1296 (2019).

[28] H. Sun, Z. Yan, F. Liu, W. Xu, F. Cheng, and J. Chen, Self-supported transition-metal-based electrocatalysts for hydrogen and oxygen evolution, Adv. Mater. **32**, 1806326 (2020).

[29] J. Kibsgaard, Z. Chen, B. N. Reinecke, and T. F. Jaramillo, Engineering the surface structure of MoS_2 to preferentially expose active edge sites for electrocatalysis, Nat. Mater. **11**, 963 (2012).

[30] Y. Li, H. Wang, L. Xie, Y. Liang, G. Hong, and H. Dai, MoS_2 nanoparticles grown on graphene: An advanced catalyst for the hydrogen evolution reaction, J. Am. Chem. Soc. **133**, 7296 (2011).

[31] K. Manthiram, B. J. Beberwyck, and A. P. Alivisatos, Enhanced electrochemical methanation of carbon dioxide with a dispersible nanoscale copper catalyst, J. Am. Chem. Soc. **136**, 13319 (2014).

[32] Z. W. Seh, J. Kibsgaard, C. F. Dickens, I. Chorkendorff, J. K. Nørskov, and T. F. Jaramillo, Combining theory and experiment in electrocatalysis: Insights into materials design, Science **355**, 6321 (2017).

[33] J. D. Benck, T. R. Hellstern, J. Kibsgaard, P. Chakthranont, and T. F. Jaramillo, Catalyzing the Hydrogen Evolution Reaction (HER) with molybdenum sulfide nanomaterials, ACS Catal. **4**, 3957 (2014).

[34] F. W. Campbell and R. G. Compton, The use of nanoparticles in electroanalysis: An updated review, Anal. Bioanal. Chem. **396**, 241 (2010).

[35] H. Le, C. Lin, E. Kätelhön, and R. G. Compton, Single-entity electrochemistry: Diffusion-controlled transport of an analyte inside a particle, Electrochim. Acta **298**, 778 (2019).

[36] M. López-Tenés, E. Laborda, A. Molina, and R. G. Compton, Guidelines for the voltammetric study of electrode reactions with coupled chemical kinetics at an arbitrary electrode geometry, Anal. Chem. **91**, 6072 (2019).

[37] R. B. Schoch, J. Han, and P. Renaud, Transport phenomena in nanofluidics, Rev. Mod. Phys. **80**, 839 (2008).

[38] S. Chen, Y. Liu, and J. Chen, Heterogeneous electron transfer at nanoscopic electrodes: Importance of electronic structures and electric double layers, Chem. Soc. Rev. **43**, 5372 (2014).

[39] Y. Liu, H. Jiang, and Z. Hou, Local field induced mass transfer: New insight into nano-electrocatalysis, Chem. Eur. J. **27**, 17726 (2021).

[40] H. Jiang, Z. Hou, and Y. Luo, Unraveling the mechanism for the sharp-tip enhanced electrocatalytic carbon dioxide reduction: The kinetics decide, Angew. Chem., Int. Ed. **56**, 15617 (2017).

[41] Y. Liu, H. Jiang, and Z. Hou, Hidden mechanism behind the roughness-enhanced selectivity of carbon monoxide electrocatalytic reduction, Angew. Chem., Int. Ed. **133**, 11233 (2021).

[42] Q.-X. Chen, Y.-H. Liu, X.-Z. Qi, J.-W. Liu, H.-J. Jiang, J.-L. Wang, Z. He, X.-F. Ren, Z.-H. Hou, and S.-H. Yu, Ordered nanostructure enhances electrocatalytic performance by directional micro-electric field, J. Am. Chem. Soc. **141**, 10729 (2019).

[43] M. Liu, Y. Pang, B. Zhang, P. De Luna, O. Voznyy, J. Xu, X. Zheng, C. T. Dinh, F. Fan, C. Cao *et al.*, Enhanced electrocatalytic CO_2 reduction via field-induced reagent concentration, Nature (London) **537**, 382 (2016).

[44] W. Sheng, H. A. Gasteiger, and Y. Shao-Horn, Hydrogen oxidation and evolution reaction kinetics on platinum: Acid vs alkaline electrolytes, J. Electrochem. Soc. **157**, B1529 (2010).

[45] M. Wang, L. Wan, J. Cheng, and J. Luo, Scalable preparation of a cuo nanosheet array via corrosion engineering for selective C–C coupling in CO_2 electroreduction, J. Mater. Chem. A **10**, 14070 (2022).

[46] A. H. da Silva, S. J. Raaijman, C. S. Santana, J. M. Assaf, J. F. Gomes, and M. T. Koper, Electrocatalytic CO_2 reduction to C_{2+} products on Cu and CuxZny electrodes: Effects of chemical composition and surface morphology, J. Electroanal. Chem. Interfacial Electrochem. **880**, 114750 (2021).

[47] A. Nitzan and L. Brus, Theoretical model for enhanced photochemistry on rough surfaces, J. Chem. Phys. **75**, 2205 (1981).